

Thermal Behavior and Microstructure Evolution during Laser Deposition with Laser-Engineered Net Shaping: Part II. Experimental Investigation and Discussion

B. ZHENG, Y. ZHOU, J.E. SMUGERESKY, J.M. SCHOENUNG, and E.J. LAVERNIA

The thermal behavior during laser-engineered net shaping (LENS) processing was numerically simulated using the alternate direction explicit finite difference method in Part I of this work. In this article, Part II, the numerical simulation results were compared to experimental results obtained with LENS-deposited 316L stainless steel. In particular, the cooling rate that is present during LENS deposition was established on the basis of dendrite arm spacing (DAS) measurements with and without a melt pool sensor (MPS) and a Z-height control (ZHC) subsystem. The microstructure of the deposited materials was characterized and analyzed, and the corresponding microhardness was measured as a function of distance from the substrate. The influence of thermal history on microstructure evolution was analyzed and discussed based on both modeling and experimental results. The results discussed in this article suggest relatively good agreement between experiments and modeling.

DOI: 10.1007/s11661-008-9566-6

© The Minerals, Metals & Materials Society and ASM International 2008

I. INTRODUCTION

A two-part investigation is described in the present work aimed at providing insight into the relationship between thermal conditions and microstructural evolution during laser-engineered net shaping (LENS)* deposition.

*LENS is a trademark of Sandia National Laboratories, and is commercialized by Optomec, Inc., Albuquerque, NM.

In Part I,^[1] we described the numerical framework used to predict the thermal profile that is present during LENS processing. More specifically, an alternate-direction explicit (ADE) finite difference formulation was used to establish the influence of laser output power, travel speed, and initial temperature of the substrate on the resulting thermal profile characteristics within deposited materials, notably the maximum temperature and cooling rate at various locations and times during LENS deposition. It was predicted that the deposition of individual layers leads to thermal fluctuations that appear as periodic pulse waves, and that the amplitude of wave peak temperature tends to dampen as more layers are deposited. High cooling rates of 10^3 to 10^4 K/s can be achieved during the initial stages of deposition, and the rapid quenching effect decreases with thickening due to heat accumulation in the deposited

materials. In Part II, we describe a series of experiments completed with LENS-deposited 316L, in an effort to provide experimental validation to the numerical results, as well as to provide insight into microstructural evolution.

It is well established that cooling rate has a profound effect on the microstructure evolution of stainless steel alloys.^[2-6] For example, five modes of solidification and twelve morphologies of Fe-Ni-Cr stainless steels were observed during the different solidification processes with different cooling rates.^[3] High cooling rates can be produced by high power density welding, resulting in microstructures that are far from equilibrium. The temperature profile surrounding the melt pool of 316L fabricated parts were measured by Hofmeister *et al.*,^[4] and the cooling rates at the solid-liquid interface ranged from 10^2 to 10^5 K/s. In the case of LENS processing, the thermal field is influenced by several interrelated variables, such as laser power, displacement speed, and powder flow rate, and accordingly, the cooling profile is complex and poorly understood.

The relationship between dendrite arm spacing (DAS) and cooling rate provides a useful approach to establish the precise effect of thermal conditions on microstructure. The relationship between second dendrite arm spacing (SDAS) and cooling rate has been experimentally determined for a number of alloy systems and, accordingly, there is extensive data available.^[7-15] The general relationship between cooling rate and SDAS is^[16,17]

$$\text{SDAS} = A(\dot{T})^{-n} \quad [1]$$

where \dot{T} is cooling rate (K/s) and A and n are constants that depend on the particular alloy system being studied. Table I shows some A and n values for different alloys from the literature.^[7-15] The calculated cooling rate for

B. ZHENG, Postdoctoral Researcher, Y. ZHOU, Associate Researcher, J.M. SCHOENUNG, Professor, and E.J. LAVERNIA, Dean of College of Engineering, are with the Department of Chemical Engineering and Materials Science, University of California, Davis, CA 95616. Contact e-mail: bzheng@ucdavis.edu J.E. SMUGERESKY, Senior Staff Member, is with Sandia National Laboratories, Livermore, CA 94551-0969.

Manuscript submitted October 22, 2007.

Article published online June 24, 2008

Table I. Values of Constants A and n Used in Equation [1]

Researcher	A	n	Materials	Condition
Lavernia <i>et al.</i> ^[8]	50	0.3	Al alloy	deposit
Caceres <i>et al.</i> ^[9]	49.0	0.42	Mg-8 pct Al-0.7 pct Zn	casting
Labrecque <i>et al.</i> ^[10]	49.9	0.34	AZ91 Mg alloy	casting
Dube <i>et al.</i> ^[11]	35.5	0.31	AZ91D Mg alloy	casting
Stone <i>et al.</i> ^[12]	50	0.33	Al-4 wt pct Cu	powder
Mizukami <i>et al.</i> ^[13]	100	0.35	Fe alloy	deposit
Joly <i>et al.</i> ^[14]	39.8	0.3	Ni superalloys	powder
Katayama ^[15]	25	0.28	310SS	1st DAS
Katayama ^[15]	80	0.33	310SS	2nd DAS

310 type stainless steel varied from 7 K/s for the casting to 7.5×10^6 K/s for the highest speed electron beam surface melting.^[3]

High cooling rates allow less time for lateral diffusion of the rejected solute and therefore require smaller DAS to avoid constitutional supercooling. Thus, nonequilibrium microstructures can develop during rapid solidification processing,^[16] and more specifically during laser-based processing.^[4,18–21] In the presence of a high cooling rate, secondary dendrite arms do not grow, as occurs in cellular or degenerate dendrite solidification. In this case, the observed DAS, instead of the conventional SDAS, is known to depend on the thermal gradient and correlates with the cooling rate in the solidifying material.^[22,23]

Previously published experimental and numerical studies on LENS deposition have shown that the temperature of a deposited component can increase during deposition due to heat accumulation.^[1,19,20] The melt pool size is proportional to the laser power input, and the overall deposition distance increases with decreasing traverse speed. During LENS deposition, maintaining consistent melt pool size and deposition distance is critical, in particular, as far as the microstructural homogeneity and dimensional accuracy of the components. Accordingly, it is necessary to provide proper thermal management of the melt pool during deposition. This can be achieved by two means: one is proper choice of process parameters; another is *via* the implementation of external sensor and control strategies to ensure that the melt pool size and deposited thickness are stable during the course of deposition.^[24] Therefore, a real time melt pool sensor (MPS) and a Z-height control (ZHC) subsystems have been developed and applied to our LENS experiments, as shown in Figure 1.

The developed MPS subsystem is designed to automatically adjust the laser input power level to maintain a constant surface area of the molten pool, which is useful for the deposition of variable materials as well as for eliminating melt pool size variations that can occur due to geometrical changes in the component. The developed ZHC subsystem is designed to automatically retain the same deposition distance by changing the laser travel speed. The challenge of controlling microstructure and component dimensions requires a quantitative understanding of the relationship between process parameters (such as laser output power and travel speed), dimension, cooling rate, microstructure, and properties by

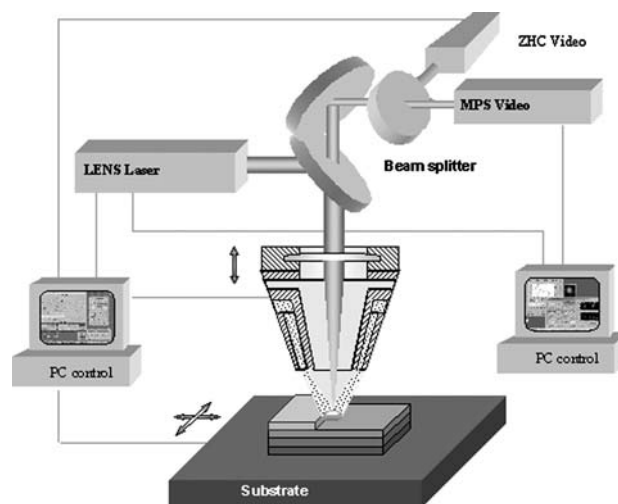


Fig. 1—Schematic of real time MPS and ZHC system applied to the LENS process.

developing a fundamental understanding of the associated transport phenomena. Therefore, the objective of this study is to experimentally validate the calculated cooling rates, and describe the effects of thermal behavior on the morphological features of microstructure that developed during LENS deposition. The correlation between thermal history, microstructure, and properties of the deposited components with and without MPS and ZHC (closed-loop/open-loop) are analyzed and reported in this article.

II. EXPERIMENTAL PROCEDURES

As-received gas-atomized 316L SS (C < 0.03 pct, Si0.7 pct, Mn1.7 pct, Mo3 pct, Ni11 pct, Cr18 pct, balance Fe) powder with a size range of 45 to 150 μm in diameter was used as feedstock material. Bulk samples were prepared by melting the feedstock powder using the focused laser beam and deposition of the melt in a layer-by-layer fashion on the substrate of 316L SS plate with a thickness of 6.35 mm, which was degreased and cleaned using acetone and ethanol before deposition.

The LENS system used in this study consists of a continuous-wave (CW) mode Nd:YAG laser operating to 650W, a four-nozzle coaxial powder feed system, a controlled environment glove box, and a motion control

Table II. Process Parameters and Mean Intercept Length λ of Cell

Sample		A	B	C
Closed-loop sensor		ZHC and MPS off	ZHC on	MPS on
Laser output power (W)		395	395	~395
Stage travel speed (mm/s)		12.7	~12.7	12.7
Powder feed rate (g/min)		10	10	10
DAS at top of sample	λ_{fine} (μm)	1.44	1.69	1.38
	λ_{coarse} (μm)	2.65	2.75	2.44
DAS at bottom of sample	λ_{fine} (μm)	1.36	1.35	1.31
	λ_{coarse} (μm)	2.41	2.43	2.38

system. The nominal laser beam diameter is 6.3 mm and has a <0.5-mm diameter circular beam waist at the focal zone with a Gaussian intensity distribution. The energy density used in the present experiment was in the range of 10^5 to 10^7 W/cm². Two powder hopper feeders can be used to deliver powders separately, and their feed rates are computer controlled individually by regulating the motor rotational speed in each powder feeder. In the case of the experiments reported herein, only one powder feeder was used.

The entire process was carried out in an Ar environment to minimize oxidation during deposition. The main process variables used for the present study were laser output power P , laser travel speed v , and powder feed rate F . Information on the process variables used in the present study is summarized in Table II.

The microstructure of laser-deposited 316L SS samples was examined *via* scanning electron microscopy (SEM) using a PHILIPS** XL-30 SFEG. The samples

**PHILIPS is a trademark of Philips Electronic Instruments Corp., Mahwah, NJ.

for metallographic examination were prepared using standard techniques. The polished surface was etched using an electrolytic etching method. The electrolyte consisted of 10 g oxalic acid and 100 mL distilled water. The etching was performed to delineate the austenite cell boundaries for 20 seconds with a voltage of 3 to 6 V. Grain or interdendrite spacing was measured by the linear intercept technique. Microhardness was measured with a force of 100 kg with a Buehler MicroMet 2004 apparatus (Buehler Ltd., Lake Bluff, IL). According to ASTM standard E8, tensile testing was conducted at a test speed of 10^{-3} /s at ambient temperature with an Instron 8801 apparatus (Instron Inc., Norwood, MA). The test specimens were machined from the center of LENS-deposited coupons, producing round dogbone-shaped specimens with a gage length of 16 mm and diameter of 3.2 mm for the tensile test. Prior to testing, the surfaces of the specimens were ground and polished to remove surface defects.

III. RESULTS AND ANALYSIS

The solidification microstructures of LENS-deposited 316L SS are complex and varied as one might expect for

the case of a melt-pool rapidly solidified microstructure. In general, a dendritic microstructure with columnar growth morphology predominates near the interface of the molten pool, which is clearly shown in Figure 2. Figure 2(a) shows the typical cross-section microstructure perpendicular to the laser travel direction and substrate obtained with optical microscopy, which reveals the inhomogeneity of the melt pool. The characteristic rows and layers of the LENS material reflect solidification from the continuously moving laser melt pool tracks.

In Figure 2(b), strong evidence of epitaxial growth off the prior solid interface can be observed within each layer. Figure 2(c) is a magnified view of a fine columnar structured region, and Figure 2(d) is a magnified view of a coarse columnar structured region shown in Figure 2(b), which displays the typical columnar dendrite structure grown toward the top center of the melt pool. Around the center, there is also a small fine equiaxed structure zone, which is the cross section of columnar dendrites parallel to the laser travel direction. The grain size at the boundary of the solidified melt pool is obviously coarser than that inside the solidified molten pool due to remelting and heat effect of the previous deposited materials with a relatively lower cooling rate.

During melt solidification, the crystals grow perpendicularly to the solidification front, which corresponds to the maximum temperature gradient.^[16,23] Equiaxed and columnar crystals are the two types of grain morphologies that can be formed during melt pool solidification of a metal. A columnar structure is formed due to a heat flux that is unidirectionally oriented (at least locally) perpendicular to the interface of the melt pool. During columnar crystal growth, the heat flows from the superheated melt into the cooler solid. The growth of a columnar crystal follows the maximum temperature gradient. On one hand, dendrites always try to grow in a direction as near normal to isotherms as their crystallography allows. On the other hand, an equiaxed structure is formed due to the growth of crystal nuclei in an undercooled isothermal melt, *i.e.*, it proceeds equally in all directions and so does the local heat flux. The transition from predominantly columnar crystal growth to equiaxed growth is due to the high amount of segregation associated with the final stages of solidification.

There is initially a steep temperature gradient in the melt pool because the temperature beneath the laser beam is high, and the substrate is an efficient heat sink. The LENS processing is essentially a dynamic process

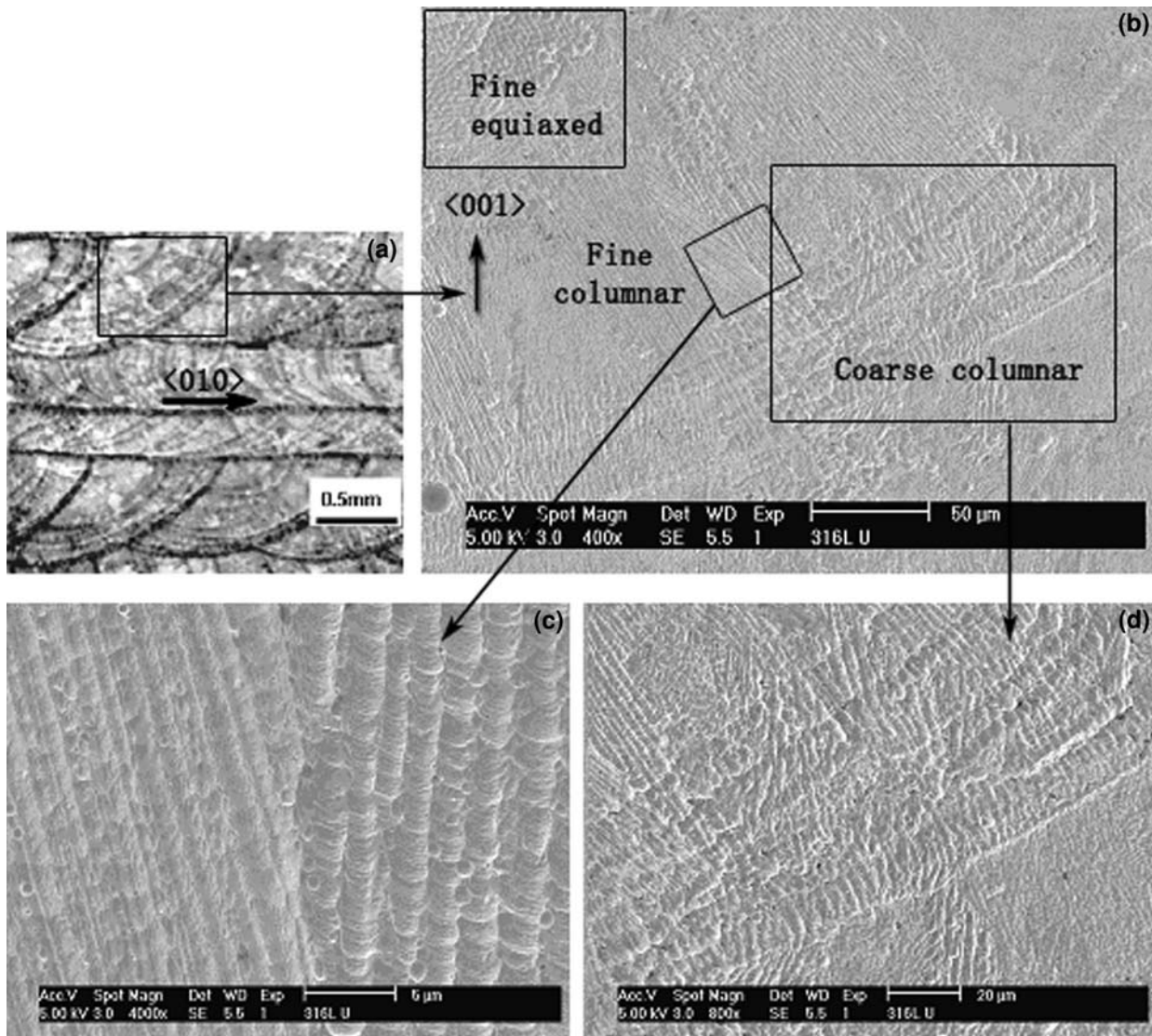


Fig. 2—(a) through (d) Laser track cross-sectional microstructures of deposited 316L stainless steel.

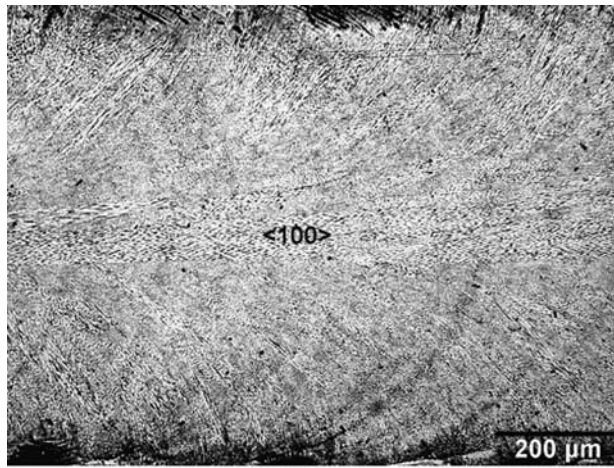
because the heat source is continuously moving. As the laser beam moves away, the maximum temperature gradients are constantly changing direction. The growing columnar crystals are thus trying to follow the maximum temperature gradients while still maintaining their preferred $\langle 100 \rangle$ direction, as shown in Figure 3, the upper surface microstructure of laser scanning track and crystal growth. This can result in changes to the crystal growth direction. The change in crystal growth direction at the melt pool center is due to the solidification front trying to keep pace with the moving laser beam. Because the crystal growth velocity attempts to keep pace with laser travel velocity, the velocity of the solidification front can be given by

$$R = v \cdot \cos \theta \quad [2]$$

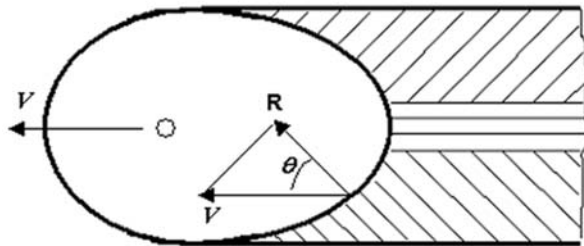
where θ is the angle between the scan direction and the growth direction, and v is the laser travel speed. The vector of R representing crystal growth rate needs to

continuously adjust itself as growth proceeds toward the laser track centerline. From Eq. [2], the solidification rate is largest when θ is about zero. The initial crystal growth rate is low and associated with a planar solidification front, and the front changes to cellular as the growth rate increases. Another reason for the local change in columnar growth direction is that renucleation occurs from the fragments of dendrite arms, which are fractured and dispersed by the turbulent convection in the melt pool. Variations in the laser travel speed can also influence the columnar direction since the growing crystals try to follow the highest temperature gradients.

Figure 4 is a magnified view of the top surface showing the microstructure of the cross section parallel to the substrate surface. It reveals a typical fine solidification cellular microstructure, which represents the cross section of the columnar dendrites, as shown in Figure 2(b). The morphology is primary austenite cells with intercellular ferrite presented at the cell boundary



(a)



(b)

Fig. 3—(a) Upper surface microstructure of laser deposition track and (b) an illustration of columnar crystal growth.



Fig. 4—Upper surface optical micrograph showing austenite solidification cellular microstructure including positions VP and VA to the axis of the columnar.

triple points and cell walls. Since 316L is an austenitic stainless steel, austenite formed extensively and was the primary phase formed during the solidification process. Rejection of solute at the solidifying interface will enrich the intercellular regions with chromium and molybdenum.^[4] Compositional variations caused by microsegregation at the boundaries outline the austenite cells by etching darker than the interior of the cells. The ferrite

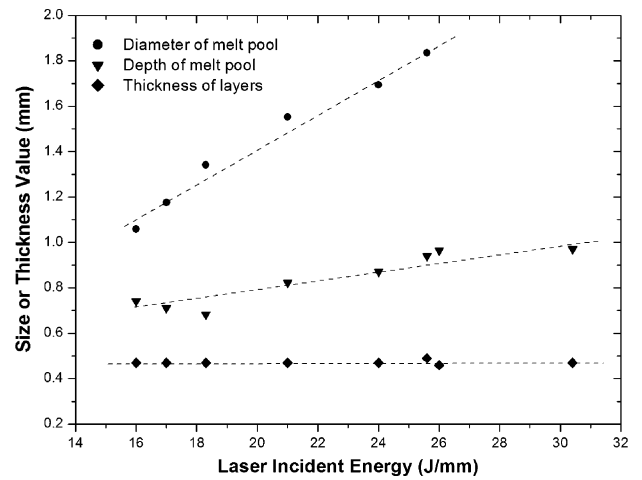


Fig. 5—Variation in melt pool dimension with laser incident energy.

content decreases with increasing cooling rate because of the reduced time for solute redistribution at high rates.^[3] The overall appearance of the microstructure is a regular array of cells appearing as a mesh. When viewed perpendicular (VP) to the axis of the columnar, the austenite boundaries appear as a hexagonal cells, and when viewed at an angle (VA) to the axis of the columnar, the austenite boundaries can be elliptical or long parallel laths in shape at high cooling rates.

Laser output power and laser travel speed played significant roles in determining the final dimensions of the deposited components. It was noted that reducing the laser power subsequently reduces the melt depth and reduces the build-up rate. The build-up height increases were nearly linear with increasing laser incident energy (laser output power divided by laser travel speed). Figure 5 shows the variation in melt pool dimension with laser incident energy. The width and depth (size) of the melt pool increase with increasing laser incident energy due to the melt pool receiving more energy, and therefore increasing in size and temperature. However, the deposited thickness for each layer does not change (about 0.4 mm), since there is remelting of previously deposited layers, which helps to develop strong metallurgical bonding between deposited layers.

The SEM studies showed various proportions of the columnar structure at different locations in the sample. A fine structure (1.2 to 2.4 μm) was found in the layers near the substrate, which then became coarser (1.5 to 3.0 μm) in the later deposited layers. The fine scale of the microstructure, evident from Figure 2, is attributed to the rapid solidification velocities, which resulted from the high cooling rate present during LENS processing, which can be determined by measuring the DAS. The DAS, λ , of different positions was measured 10 times, and a mean value of the measurements was used, as reported in Table II.

Relationships between the DAS λ (μm) and cooling rate \dot{T} (K/s) have been developed, and these show that a linear relationship exists between $\log \lambda$ and $\log \dot{T}$.^[16] Equation [3] is an experimental relationship between the cooling rate \dot{T} and the DAS λ for 316L SS^[15]

$$\lambda = 80\dot{T}^{-0.33} \quad [3]$$

The cooling rate is determined to be in the range of 10^3 to 10^4 K/s, as shown in Figures 6 and 7, which is in agreement with the numerical simulation results discussed in Part I^[1] of this work. The cooling rates experienced by laser-deposited 316L SS samples generally decrease with increasing distance from substrate due to the heat accumulation and mass build up during deposition. The higher temperature of previously deposited layers effectively decreases the cooling rate by decreasing the thermal gradient between the melt pool and the surrounding solid. It was also found that both a finer microstructure and a higher cooling rate were obtained by decreasing the laser output power and increasing the laser travel speed, for the range of values studied herein.

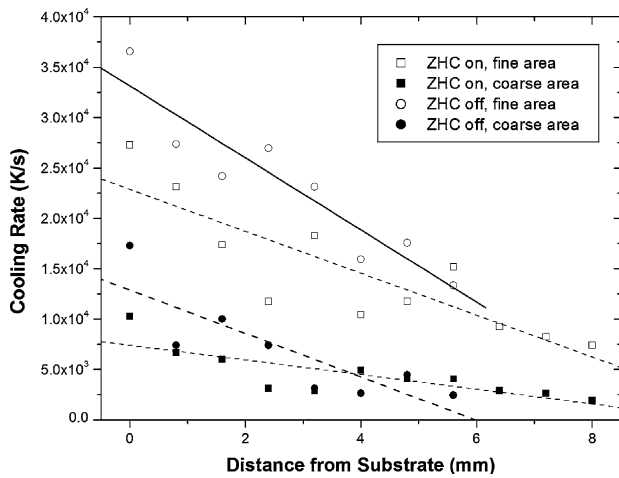


Fig. 6—Variation in cooling rate vs distance from substrate with or without ZHC.

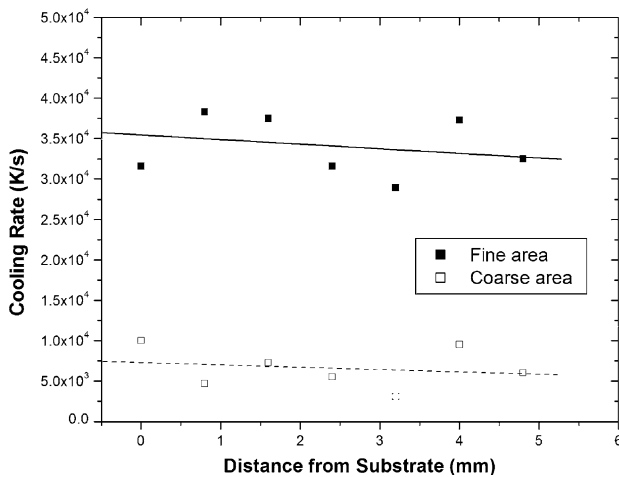


Fig. 7—Variation in cooling rate vs distance from substrate with MPS.

Published experimental and numerical results^[1,20] show that the thermal excursions dampen out when the energy source moves away from the substrate during deposition. After the initial temperature peak, the heat is quickly dissipated away, leaving a thermal increase of about 100 K for the first layer. This initial thermal transient leads to a rapid quenching effect at the initial deposition stage, ultimately yielding a harder material (Figure 8). The microhardness values decrease with increasing distance from the substrate for both cases, with or without ZHC, which suggests that while the ZHC function can improve the accuracy of deposit dimension, it does not help to improve the microstructural homogeneity.

Using the MPS, however, leads to a more uniform microstructure and microhardness of deposited materials (Figure 9), comparing the cooling rate variation shown in Figure 7. The cooling rate is inversely proportional to

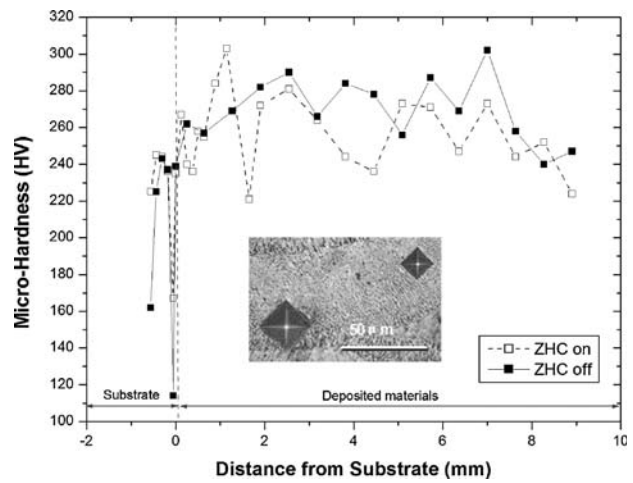


Fig. 8—Variation in microhardness vs distance from substrate with or without ZHC.

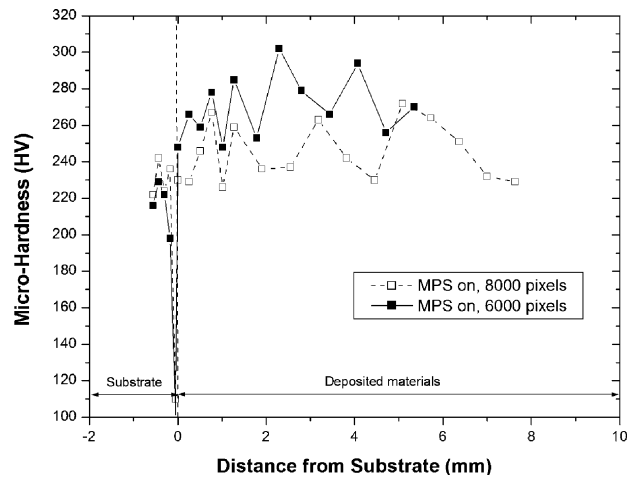


Fig. 9—Variation in microhardness vs distance from substrate with MPS.

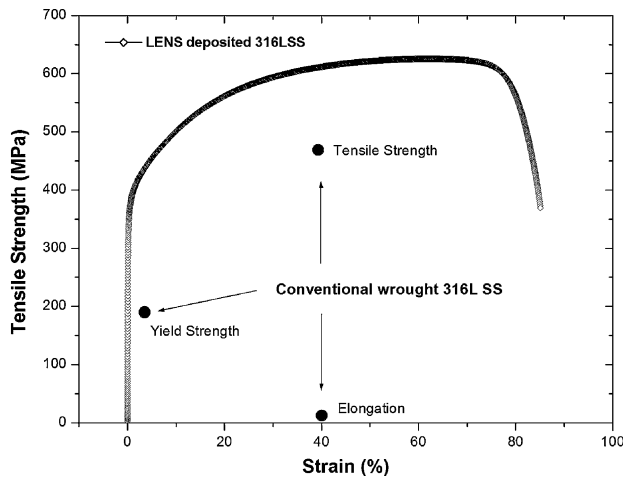


Fig. 10—Comparison of tensile mechanical properties for LENS-deposited and conventional wrought 316L SS.

the power level used in the experiments. Thus, the higher quench rates are available at the lower laser power output when a small molten pool size setting is used. When a higher laser power is used, significantly coarser dendrites are evident, which is consistent with the lower microhardness values shown in Figure 9. Hence, the application of the melt pool sensor control improves the homogeneity of the solidified microstructure, and results in more uniform properties of the deposited materials. Figure 10 shows the tensile test results for the LENS-deposited 316L SS sample compared with those of conventional wrought 316L SS.^[25] The yield strength is more than 25 pct higher than that of wrought 316L SS, while the ductility is 100 pct higher than that of wrought 316L SS. The improvement in strength is attributable to the overall refinement in microstructure of the LENS-deposited material. For example, LENS-processed grain sizes range from 1 to 5 μm , whereas the grain sizes for conventional wrought 316L SS are 40 to 50 μm .^[19] The influence of grain size on the deposited 316L SS strength can be expressed by the Hall–Petch equation:^[23]

$$\sigma_g = \sigma_0 + k_y \cdot d^{-1/2} \quad [4]$$

where σ_0 is the conventional strength of 316L SS alloy, k_y is the empirical constant, and d is the grain size. When grain size decreases from 45 to 3 μm , the strength increases to about 3.87 times that of conventional wrought strength. Whereas the computed value should be interpreted as an upper bound, it does confirm the importance of grain size. In fact, there are other microstructural artifacts and defects, such as porosity and segregation, which will influence the actual properties of deposited 316L SS alloys. The documented increase in ductility may be attributed to the presence of a columnar structure parallel to the tensile direction. The weavelike texture of microstructure formed during LENS processing, as shown in Figures 2 and 4, also likely contribute to the higher strength and ductility of LENS-deposited 316L SS. In a normal LENS

processing, the direction of laser travel changes frequently. The laser movement direction is perpendicular to each consecutive two layers, and each layer also has a complex columnar structure, which forms the observed weavelike texture of microstructure. This type of microstructure may be beneficial in terms of fracture toughness, creep resistance, and lower fatigue crack growth rate.^[26] The discrete additive nature of the LENS process also results in a cyclic thermal environment as each pass reheats the previously deposited material. Solid-state transformations are likely to occur during this complex thermal cycling, possibly leading to some tempering and aging effects.

IV. DISCUSSION

Similar to most other additive processes, LENS laser deposition involves numerous thermal heating and cooling cycles consisting of heating of deposited structure by newly deposited metal and cooling after the newly deposited layer is solidified, as shown in the modeling results of Figure 4 in Reference 1. Thus, the goal of any assessment of microstructural evolution is to determine the response of the alloy to these thermal cycles.

There are two trends in the temperature of the deposited materials during laser deposition with LENS. First, the peak temperature decreases with increasing number of deposition cycles as a result of an increase in the distance between the molten pool and the bottom surface. Second, the temperature at the end of each deposition interval, corresponding to slow cooling, increases with increasing cycle number as a result of the increased substrate temperature. It is noted that when the cycle number reaches a certain value, the increase in temperature change at the bottom surface of the deposited material decreases, as shown in the modeling results in Figure 7 of Reference 1, indicating that the LENS process attains a quasi-steady state.

During deposition, when a new layer impinges onto the growing deposited material's surface, it is convenient to divide its cooling process into two different stages: before and after the thermal equilibrium between the new deposited layer and the previously deposited material. This process can finish within one time interval under certain parametric conditions. Prior to attaining thermal equilibrium, cooling is relatively fast (approximately 10^2 to 10^4 K/s), due to the rapid heat conduction across the interface between the new layer and the previously deposited material. This phenomenon is analogous to rapid quenching. As a result, the cooling rate of the new deposited layer is initially very high (the modeling results in Figure 5 of Reference 1). However, after thermal equilibrium is attained, cooling depends on the cooling environment of the local material and is usually slow, as shown in the modeling results in Figure 6 of Reference 1.

If the temperature at the surface is lower than the solidus temperature at the end of a time interval, the deposited layer is completely solidified and the solidification front reaches the deposited material's surface prior to arrival of the next layer. In this case, the

quenching effect is significant. In the initial stage of deposition, since the substrate and deposited materials remain at a low temperature, and heat is quickly dissipated from the deposited material to the substrate, the preceding layers have completed their solidification prior to the arrival of the following ones. In this case, the rapid quenching dominates the overall cooling process of the layers. It is well known that microstructural characteristics strongly depend on the cooling rate during solidification. As a result, the microstructure of the initially deposited material is, to a large extent, related to this rapid solidification process, and a fine microstructure is obtained with high strength property, as shown in Figures 6 and 8.

The temperature of deposited materials monotonically increases with increasing thickness. The temperature at the end of a deposited upper layer is much higher than that of a lower layer, as shown in the modeling results in Figure 7 of Reference 1. For the case consisting of a short time interval, a high laser power input, and a high substrate preheat temperature, the temperature at the end of each cycle increases rapidly, as shown in the modeling results in Figures 9 through 11 of Reference 1. If the temperature on the upper surface of the current deposited layer remains above the solidus temperature, even after the arrival of the next layer, the current layer has not solidified completely, which implies that the solidification front has lagged behind the deposited material's surface. As a result, a mushy layer begins to form at the top portion of the deposited material. After that, the deposited material's surface remains in a mushy state even after the arrival of the next layer. This condition is commonly reported for spray forming,^[27,28] but seldom occurs during laser deposition due to its very fine melt pool and slow deposition rate. Although cooling is initially fast due to the rapid quenching effect, it leads to only partial solidification during that time period. After having reached thermal equilibrium, the local cooling rate environment determines solidification, and this is generally slow. Thus, the later thermal history gradually plays an important role in the cooling process of the upper deposited layer. In addition, if the top surface remains in a mushy state, it is difficult to control component geometry. As the temperature at the deposited material's surface is very close to the initial temperature of incoming layers, the rapid quenching effect disappears, and a slow cooling environment dominates the overall cooling process of upper deposited layers.

The differences in the cooling process are expected to cause microstructural differences between different regions within the deposited material, which have been confirmed by a number of experimental observations.^[29–31] During deposition, the incoming layers are not only the mass source, but also the energy source. The later incoming layers always affect the cooling process of the previously deposited material. Such as after the fifth layer is deposited, the initial layer still experiences a thermal excursion. This complicated thermal cycling affects the material properties, including residual stress and mechanical strength, due to tempering or aging

effects. One common result is that the grains are finer in the bottom region of the deposited material and become coarse in the region away from the substrate (Figure 6). Therefore, the developed MPS sensor is useful for eliminating melt pool size variations and improving microstructural homogeneity by automatically adjusting the laser input power to maintain a constant size of the molten pool.

During laser deposition, there is always remelting of previously deposited materials, which is important to the formation of a fully dense component. As the remelting occurs, the boundaries between the deposited layers disappear, and the effects of the interface heat transfer coefficient are not significant. Since the temperature at the deposited material's surface increases with thickness, the remelting also increases with thickness. In the remelted region, therefore, porosity should decrease with deposited material thickness. Experimental observations have shown that porosity is relatively high in the initially deposited material, and decreases with increasing distance from the substrate,^[32] which is in agreement with the previous arguments. The primary cause of gas porosity is that gas dissolved or entrapped in the melt may not have sufficient time to escape to the top of the molten pool due to rapid solidification rates during LENS deposition, therefore forming gas porosity in deposited components. The possible gas sources include surface entrainment during particle impact into the molten pool, contamination by powder delivery gases, and vaporization of deposited alloy caused by high intense energy of laser beam. It was also reported that the decrease of residual gas in the starting powder is helpful to decrease the porosity in laser-deposited materials.^[33] In addition, disturbed flow in the melt pool could give rise to high porosity, while steady flow could give rise to low porosity. Further studies aimed at understanding the mechanisms that govern the evolution of pores during LENS deposition are necessary.

V. CONCLUSIONS

The results described in the present article lead to the following conclusions.

1. Fully dense metallic parts with fine microstructures of 316L stainless steel can be directly formed without tooling through laser melting of coaxially-fed powders. Metallographic examination showed that austenite grows epitaxially from the previously deposited metals at layer boundaries.
2. The microstructure evolution during LENS processing is generally complex due to the multiple thermal reheating cycles, which have significant effects on the thermal environment. The cooling rate experienced by the deposited materials decreases with concomitant coarsening of the microstructure as the thickness of the deposited material increases.
3. The ZHC system controls the deposited layer height by changing the stage traverse speed, and consequently has a less important effect on the properties of deposited materials. The MPS controls the melt

pool size *via* control of the laser output power level, thereby improving microstructure homogeneity.

4. Experimental results showed that the cooling rate experienced by deposited materials initially varied from 10^3 to 10^4 K/s, which is consistent with numerical simulation results, and that the microhardness values of laser-deposited 316L stainless steel can reach 300 HV (3.18 GPa).
5. The laser deposition of multiple layers of 316L SS results in a unique microstructural morphology, which leads to improvements in mechanical properties relative to those of the conventional wrought material.

ACKNOWLEDGMENTS

This work was supported by the National Science Foundation (Grant No. DMI-0423695) and by NASA Marshall (Contract No. NNM06AB11C). Work at Sandia National Laboratories is supported by the United States Department of Energy (Contract DE-AC04-94AL85000).

REFERENCES

1. B. Zheng, Y. Zhou, J.E. Smugeresky, J.M. Schoenung, and E.J. Lavernia: *Metall. Mater. Trans. A*, 2008, vol. 39A, DOI: [10.1007/s11661-008-9557-7](https://doi.org/10.1007/s11661-008-9557-7).
2. S.A. David, J.M. Vitek, and T.L. Hebble: *Weld. J.*, 1987, vol. 66 (10), pp. 289–300.
3. J.W. Elmer, S.M. Allen, and T.W. Eager: *Metall. Mater. Trans. A*, 1989, vol. 20A, pp. 2117–31.
4. W. Hofmeister, M. Griffith, M. Ensz, and J. Smugeresky: *JOM*, 2001, vol. 53, pp. 30–34.
5. J.E. Smugeresky, B. Zheng, Y. Zhou, and E.J. Lavernia: *TMS'06*, San Antonio, TX, Mar. 12–16, 2006.
6. B. Zheng, Y. Zhou, J.E. Smugeresky, and E.J. Lavernia: *Proc. Powder Metall.*, 2006, pp. 81–94.
7. I.C. Stone and P. Tsakiroopoulos: *Int. J. Rapid Solidification*, 1992, vol. 7, pp. 177–90.
8. E.J. Lavernia: Ph.D. Dissertation, MIT, Cambridge, MA, 1986, p. 58.
9. C.H. Cáceres, C.J. Davidson, J.R. Griffiths, and C.L. Newton: *Mater. Sci. Eng. A*, 2002, vol. 325, pp. 344–55.
10. C. Labrecque, R. Angers, R. Tremblay, and D. Dubé: *Can. Metall. Q.*, 1997, vol. 36, pp. 169–75.
11. D. Dube, A. Couture, Y. Carbonneau, M. Fiset, R. Angers, and R. Tremblay: *Int. J. Cast Met. Res.*, 1998, vol. 11, pp. 139–44.
12. I.C. Stone and P. Tsakiroopoulos: *Int. J. Rapid Solidification*, 1992, vol. 7, pp. 177–90.
13. H. Mizukami, T. Suzuki, and T. Umeda: *Tetsu-to-Hagané*, 1992, vol. 78, pp. 580–86.
14. P.A. Joly and R. Mehrabian: *J. Mater. Sci.*, 1974, vol. 9, pp. 1446–55.
15. S. Katayama and A. Matsunawa: *Proc. ICALEO*, 1984, pp. 60–67.
16. M.C. Flemings: *Solidification Processing*, McGraw-Hill, New York, NY, 1974, pp. 148–54.
17. M.E. Glicksman and P.W. Voorhees: *Metall. Trans. A*, 1984, vol. 15A, pp. 995–1001.
18. W. Hofmeister, M. Wert, J. Smugeresky, J.A. Philliber, M. Griffith, and M. Ensz: *JOM*, 1999, vol. 51, JOM-e online at <http://www.tms.org/pubs/journals/JOM/9907/Hofmeister/Hofmeister-9907.html>.
19. M.L. Griffith, M.T. Ensz, J.D. Puskar, C.V. Robino, J.A. Brooks, J.A. Philliber, J.E. Smugeresky, and W.H. Hofmeister: *MRS Symp. Y. Proc.*, 2000, vol. 625, pp. 9–20.
20. M.L. Griffith, M.E. Schlienger, L.D. Harwell, M.S. Oliver, M.D. Baldwin, M.T. Ensz, J.E. Smugeresky, M. Essien, J. Brooks, C.V. Robino, W.H. Hofmeister, M.J. Wert, and D.V. Nelson: *J. Mater. Design*, 1999, vol. 20 (6), pp. 107–14.
21. S.M. Kelly and S.L. Kampe: *Metall. Mater. Trans. A*, 2004, vol. 35A, pp. 1861–67.
22. E.J. Lavernia, J.D. Ayers, and T.S. Srivatsan: *Int. Mater. Rev.*, 1992, vol. 37, pp. 1–44.
23. R.W. Cahn and P. Haasen: *Physical Metallurgy*, 3rd ed., Elsevier BV, New York, NY, 1983, p. 856.
24. J.E. Smugeresky, B. Zheng, Y. Zhou, and E.J. Lavernia: *TMS'05*, San Francisco, CA, Feb. 13–17, 2005.
25. http://www.azom.com/details.asp?ArticleID=2382#_Key_Properties.
26. M.J. Donachie: *Titanium, A Technical Guide*, 2nd ed., ASM INTERNATIONAL, Metals Park, OH, 2000, pp. 13–24.
27. E.J. Lavernia and Y. Wu: *Spray Atomization and Deposition*, John Wiley & Sons, Inc., New York, NY, 1996, pp. 311–14.
28. Q. Xu, V.V. Gupta, and E.J. Lavernia: *Metall. Mater. Trans. B*, 1999, vol. 30B, pp. 527–39.
29. A. Vasinonta, J.L. Beuth and R. Ong: *Proc. 12th Ann. SFF Symp.*, Austin, TX, Aug. 2001, pp. 432–40.
30. J.A. Brooks, C.V. Robino, T. Headley, S. Goods, R.C. Dykhuizen, and M.L. Griffith: *SFF Symp.*, Austin, TX, Aug. 1999, p. 375.
31. W.P. Liu and J.N. DuPont: *Metall. Mater. Trans. A*, 2004, vol. 35A, pp. 1133–40.
32. Y. Xiong, B. Zheng, J.E. Smugeresky, L. Ajdelsztajn, and J.M. Schoenung: *MS&T'05*, Pittsburgh, PA, Sept. 25–28, 2005.
33. D.F. Susan, J.D. Puskar, J.A. Brooks, and C.V. Robino: *Mater. Characterization*, 2006, vol. 57 (1), pp. 36–43.